Oncogene *c-Myc* Regulates Upper Respiratory Epithelial Repair for Host Immunity During Acute Influenza Infection

Alexander G. Foote[1], Le Xu[1], Jamie Verheyden[1], Belle Pan[1], Nikita Katoch[1], Xin Sun[1, 2]

[1] Department of Pediatrics, University of California, San Diego; [2] Department of Cell and Developmental Biology, University of California, San Diego

*Corresponding author. e-mail: xinsun@health.ucsd.edu

Abstract: The upper respiratory epithelium protects the airway from microbial exposure, environmental irritants, and viral pathogens such as influenza A virus (IAV). Situated at the airway–gastrointestinal junction, the larynx must integrate this barrier function with fine neuromuscular control under constant immune stimulation. Clinical syndromes such as post-viral vagal neuropathy—marked by chronic cough, throat clearing, dysphonia, and vocal fatigue—highlight critical gaps in our understanding of how the larynx and upper airway remodel after viral injury. To address this, we employed mouse models integrating genetics, imaging, and single-cell transcriptomics to dissect IAV-induced injury and repair in the upper respiratory tract. IAV infection displayed regionally restricted tropism toward ciliated, secretory, neuroendocrine, and basal epithelial cells, eliciting rapid clearance, acute neutrophil invasion, and a sustained intraepithelial population of cytotoxic $CD8^+$ natural killer T (NKT)-like cells. Single-cell analysis revealed injury-induced *Myc* expression in $KRT5^+$ basal progenitors, which activated a proliferative repair program and an epithelial–immune communication circuit centered on a MYC-dependent CXCL10–CXCR3 axis. Basal-specific *Myc* deletion preserved viral replication and clearance but blunted injury-induced proliferation, skewed lineage differentiation, and impaired $CD8^+$ NKT cell recruitment. These findings define a coordinated epithelial–immune program governing post-IAV mucosal restoration and offer mechanistic insight into persistent upper airway sequelae.

Introduction

The upper respiratory epithelium serves as a frontline barrier defense, shielding the airways from a constant barrage of symbiotic microbes, environmental irritants, and a range of invading pathogens.[1-4] Mucosal immunity is critical to maintain organ homeostasis following epithelial insult.[5,6] Among common respiratory pathogens, influenza A virus (IAV) remains a major global threat, causing substantial morbidity, acute respiratory distress, and death each year.[7] While epithelial cells exhibit significant regenerative capacity, it is not well-described how the upper respiratory epithelium remodels in post-viral settings.

The larynx represents a unique and understudied component of this system. As a neurologically complex sensorimotor organ positioned at the intersection of the respiratory and gastrointestinal tracts, the larynx must integrate epithelial defense with fine-tuned neuromuscular control amid constant immunologic challenges. Work in papillomaviral disease has highlighted this complexity: in severely immunocompromised mice, laryngeal infection with MmuPV1 leads to severe dysplasia and invasive cancer persisting for months,[8] whereas immunocompetent mice demonstrate protection against recurrent or vertical infection,[9] underscoring the importance of

epithelial–immune crosstalk in shaping local antiviral responses. Yet, beyond these models, the impact of other clinically relevant viruses—such as influenza—on laryngeal and upper airway biology remain surprisingly unexplored, with limited data on multi-organ, systems-level analysis.

Recent single-cell studies have revealed the upper respiratory epithelium to be highly compartmentalized, with distinct proximal–distal and basal–luminal transcriptional programs across the pharyngolaryngeal and tracheobronchial regions.[10] Many respiratory viruses enter through, and initially engage with, sentinel epithelial cells at these mucosal surfaces.[6] Early repair responses trigger inflammatory cascades that are central to local immune regulation and, when dysregulated, contribute to chronic disease.[1,6] Acute upper respiratory infections are among the most common illnesses globally;[11] although typically self-limiting, a subset of patients experience persistent sensory and motor dysfunction long after acute illness, suggesting systems-level changes. Post-viral vagal neuropathy exemplifies this phenomenon, often manifesting as chronic cough, throat clearing, dysphonia, vocal fold paresis, and vocal fatigue.[12-17] Despite strong clinical associations linking these symptoms to antecedent viral illness, the mechanisms driving post-viral laryngeal dysfunction remain undefined.

To address this gap, we sought to define the upstream cellular and molecular events that shape epithelial repair and immune activation following IAV-induced injury in the mouse upper respiratory tract. Using an integrative approach combining mouse genetics, cell-based assays, and single-cell transcriptomics, we uncovered coordinated epithelial and immune responses that extends well beyond the acute phase of infection. We show that IAV infection targeting discrete epithelial lineages (ciliated, secretory, neuroendocrine, and basal) elicits a rapid Ly6G$^+$ neutrophilic response and establishes a persistent intraepithelial population of cytotoxic CD8$^+$ NKT-like cells marked by a durable effector transcriptome. We further identify ectopic *Myc* induction within injured subglottic and tracheal pseudostratified epithelium and demonstrate that KRT5$^+$ basal progenitors deploy a *Myc*-dependent proliferative and chemokine program that shapes downstream immune behavior. Basal-specific loss of *Myc* blunts epithelial expansion and disrupts lineage differentiation, while attenuating CXCL10-dependent recruitment of CXCR3+ CD8$^+$ NKT cells. Together, these findings delineate a systems-level epithelial–immune circuit governing post-viral remodeling in the upper respiratory tract and offer mechanistic insight into clinically relevant sequelae such as post-viral laryngeal sensorimotor dysfunction.

Results

Spatial and temporal dynamics of IAV infection reveal regionally restricted epithelial tropism and rapid viral clearance. To delineate the spatiotemporal progression of IAV infection along the upper respiratory tract, we generated large-scale coronal sections encompassing the pharyngolaryngeal-to-tracheobronchial axis from wild-type (WT) mice at 1, 3, 7, and 8 days post-infection (DP-IAV) (Fig. 1A,B). Multiplex RNA in situ hybridization with probes targeting IAV transcripts and the interferon-γ-inducible chemokine *Cxcl10*—known to orchestrate antiviral immunity[18]—revealed initial viral localization to the airway epithelium at 1DP-IAV, with peak epithelial coverage at 3DP-IAV (Fig. 1C,D). Viral transcripts persisted through 7DP-IAV but were eradicated by 8DP-IAV, aligning with established timelines of innate immune-mediated clearance.[19] *Cxcl10* expression mirrored viral burden, with negligible expression at 8DP-IAV, thereby underscoring its role in recruiting effector cells to sites of active replication (Fig. 1C). Consistent with prior reports,[20] IAV induced transient morbidity with decrease in body

weight of ~20%, reaching its lowest point at 10DP-IAV before returning to near baseline levels by 21DP-IAV (Fig. 1E).

Building on this temporal framework, we interrogated regional vulnerabilities by reorienting sections along dorsal-ventral and medial-lateral axes at peak infection (3DP-IAV). Pseudostratified epithelia of the subglottis, trachea, and extrapulmonary bronchi exhibited the highest susceptibility to IAV-induced cytopathy, whereas stratified, squamous regions of the glottis and supraglottis harbored fewer infected cells (Fig. 1C; Fig. S1A). This topographic bias suggested that epithelial architecture and cell-type composition dictate viral entry and propagation.

To link infection dynamics to regenerative potential, we traced basal progenitor responses using immunofluorescence for keratins KRT5 and KRT17—hallmarks of proliferative basal cells—across acute (3–7DP), subacute (14DP), and resolution (21DP) phases (Fig. 1F). Hyperplasia of KRT5$^+$KRT17$^+$ cells emerged by 3DP-IAV, crested at 7–14DP-IAV, and normalized by 21DP-IAV (Fig. 1G–G′). Compartment-specific quantification (supraglottic surface epithelium [SE], subglottic SE, tracheal SE, and submucosal glands [SMG]) confirmed that expansion was confined to pseudostratified zones of prior viral enrichment, with maximal accrual in subglottic and tracheal epithelia (Fig. 1H; Fig. S1B). Thus, basal cell activation represents a targeted reparative program, spatially attuned to sites of epithelial compromise.

We next resolved the cellular substrates of infection through colocalization of IAV transcripts with lineage-defining markers (Fig. 1I–P). In the trachea, viral RNA predominantly colocalized with FOXJ1$^+$ ciliated and SCGB1A1$^+$ club cells (Fig. 1K), while in the laryngeal epiglottis, SCGB1A1$^+$ secretory cells were preferentially targeted (Fig. 1L). Lineage tracing in Ascl1^{CreER};tdTomato mice further implicated subglottic and tracheal neuroendocrine cells as viral reservoirs (Fig. 1M). Additionally, IAV enrichment extended to KRT13$^-$ suprabasal layers of stratified squamous hillocks and arytenoid mucosa (Fig. 1N,O), as well as dispersed KRT5$^+$Ki67$^+$ basal cells (Fig. 1P; Fig. S1C). Collectively, these data delineate a broad yet selective epithelial tropism, wherein IAV exploits regionally specialized sentinel cells to establish foothold, culminating in viral detection and progenitor-driven remodeling.

Neutrophil epithelial invasion and persistent CD8$^+$ NKT-like sentinels drive post-IAV airway immunity and repair. Given that viral clearance hinges on coordinated innate and adaptive immunity to preserve epithelial barrier function,[5] we systematically profiled immune infiltration to dissect its contributions to resolution and homeostasis. Prior studies have implicated neutrophils in early antiviral containment and CD8$^+$ T cells in late-stage cytotoxicity;[18,21] thus, we prioritized these compartments using Ly6G (neutrophil) and CD3 (pan-T cell) immunostaining in WT tissues at acute (3DP-IAV, 7DP-IAV) and chronic (21DP-IAV) stages (Fig. 2A–F). In uninfected controls, Ly6G$^+$ neutrophils resided in the subepithelial compartment. At 3DP-IAV, however, these cells invaded the pseudostratified epithelium, colocalized with IAV enriched cells, aggregating into luminal-extruding spheres suggestive of NETosis-mediated viral entrapment (Fig. 2D,D′; Fig. S1D). This breach resolved by 7DP-IAV (Fig. 2D′), indicating a temporally restricted role in acute containment.

In contrast, intraepithelial CD3$^+$ T cells accrued progressively, peaking at 7DP-IAV and remaining significantly expanded at 21DP-IAV over saline controls (Fig. 2E,F). To molecularly characterize this resident population, bulk RNA sequencing of 21DP-IAV laryngeal and tracheal tissues identified

a cytotoxic signature dominated by *Cd8a, Cd8b1, Gzma, Gzmb,* and *Ccl5* transcripts (Fig. 2G). *In situ* validation confirmed colocalization of *Gzmb*+*Ccl5*+ cells within the epithelium at 21DP-IAV (Fig. 2H). Gene Ontology (GO) analysis of differentially upregulated genes was enriched for T cell-mediated immunity (*Cd8a, Prf1*), pyroptosis (*Gzma, Gzmb*), epithelial differentiation (*Sult1b1, Dhrs9, Cdk1*), metabolic regulation (*Ccl5, Cdk1*), and apoptosis (*Gzma, Prf1, Gzmb*) (Fig. 2I), implying multifaceted contributions to both viral lysis and tissue restitution.

To integrate these immune dynamics with epithelial repair and viral hotspots, we conducted single-cell RNA sequencing (scRNA-seq) on *en bloc*-dissociated tissues along the pharyngolaryngeal-to-tracheobronchial axis from 7DP-IAV—the timepoint between peak inflammatory repair and viral clearance (Fig. 2J). Unbiased clustering resolved 13 immune subsets (Fig. 2K,L; Fig. S1E-G), with compositional shifts post-IAV dominated by T/NK lineage expansion (Fig. 2M). Notably, we identified a transcriptionally distinct CD8$^+$ NKT-like cell cluster, co-expressing canonical T cell (*Cd3d, Cd8b1*), NK (*Nkg7*), and Th1/iNKT markers (*Klrk1, Tbx21, Ifng*), alongside cytotoxic effectors (*Gzma, Gzmb, Ccl5*) (Fig. 2L,N; Fig. S1H). Consistent with a tissue-resident phenotype, these cells upregulated canonical residency markers (*Cd69, Itga1*) and mirrored transcriptional programs observed in our bulk-seq dataset (Fig. 2N,O), suggesting that CD8$^+$ NKT cells may function as durable sentinels for immune surveillance.

scRNA-seq uncovers MYC-driven proliferative basal progenitors in post-IAV epithelial repair. To dissect the epithelial regenerative repertoire during the transitional phase of IAV clearance, we interrogated EpCAM$^+$-enriched fractions from our 7DP scRNA-seq atlas (Fig. 3A). Dimensionality reduction and unsupervised clustering delineated 20 distinct transcriptional states spanning the upper respiratory epithelium (Fig. 3A–D; Fig. S1I), which segregated into laryngeal, tracheal, and SMG domains in accordance with anatomical and prior transcriptomic delineations.[10] A salient feature was the emergence of proliferative epithelial clusters, disproportionately represented in our post-IAV condition (Fig. 3B,C,E), implying a stimulus-dependent expansion or transdifferentiation program in response to viral perturbation.

To pinpoint viral niches at cellular resolution, we augmented the reference transcriptome with the complete IAV genome sequence (TableS1), enabling imputation of viral transcripts across clusters. This revealed a stark epithelial tropism, with highest *IAV*-mRNA enrichment in secretory, ciliated, and—critically—the novel IAV-enriched (e.g. responsive) subsets (Fig. 3F; TableS1), thereby validating our spatial mapping. Sporadic detection in CD8$^+$ NKT cells (<15%) and vascular smooth muscle (<5%) hinted at intercellular viral transfer or bystander activation (Fig. 3F).

To confirm that the synthetic 'IAV-gene' did not confound dimensionality reduction or clustering in our scRNA-seq analysis, we reprocessed the dataset after its exclusion, maintaining identical parameters and fixed seeds. Cell-type labels were aligned by barcode to permit one-to-one comparison. Clustering outcomes were identical, with an adjusted Rand index (ARI) and normalized mutual information (NMI) of 1.00, and a perfectly diagonal confusion matrix (TableS1). PCA embeddings (PCs 1–30) showed near-perfect congruence via Procrustes analysis (Gower's $m^2=1.26\times10^{-4}$, r=0.99994; TableS1), with gene loading vectors exhibiting high concordance (median Pearson r=0.99936 across PCs). Local topology, assessed by k-nearest neighbor (kNN) Jaccard overlap, remained unchanged (median=1.00; 10th/50th/90th percentiles: 1.00/1.00/1.00). UMAP visualizations confirmed

preservation of manifold structure and cell-type organization (Fig. S2A). These metrics collectively affirm that the synthetic 'IAV-gene' exerted no discernible influence on the transcriptomic landscape or clustering solution.

The temporal coincidence of our IAV-enriched subpopulation with peak basal hyperplasia prompted us to posit a progenitor-like identity underpinning repair. Subclustering unmasked proliferative heterogeneity, with G2/M- and S-phase signatures evoking cell-cycle traversal (Fig. 3G–I; TableS1). Preeminent among these was a basal-enriched contingent, defined by *Trp63, Krt5, Krt14, Krt17*, and *Ngfr*, and biased toward S-phase progression—hallmarks of replicative competence in response to genotoxic stress (Fig. 3G-J). Pathway analysis through irGSEA unveiled marked upregulation of MYC target gene sets in the IAV-enriched basal subpopulation (Fig. 3K), inspiring targeted follow-up experiments.

Basal-specific Myc ablation impairs proliferative repair and lineage commitment following IAV injury. The proto-oncogene transcription factor *c-Myc* (hereafter *Myc*) constitutes a central regulator of immune cell proliferation, metabolic reprogramming, and differentiation, coordinating rapid cellular responses during activation and inflammatory states.[22-24] Interrogation of our scRNA-seq dataset revealed selective enrichment of *Myc*—but not *L-Myc* or *N-Myc*—within the IAV-enriched population, with the highest expression in the basal subpopulation, where 72% of basal cells expressed *Myc* (Fig. 4A,B; Fig. S2B,C). Pseudotemporal ordering further supported a stem-like trajectory, bifurcating toward goblet, luminal-hillock, differentiating club, mature club, and stress-activated epithelial fates (Fig. 4C). Spatial validation via *in situ* hybridization confirmed widespread ectopic *Myc* expression throughout the pseudostratified epithelium spanning the subglottis, trachea, and extrapulmonary bronchi during the acute post-IAV phase (Fig. 4D). Collectively, these findings designate a MYC-driven basal cell program as a central mediator of acute epithelial regeneration following IAV injury.

To assess the functional requirement of *Myc* in epithelial repair, we generated tamoxifen-inducible basal cell–specific knockout mice (*Krt5*^{creER};*Myc*$^{flox/flox}$, hereafter *Krt5*^{creER};*Myc*). Experimental animals received three consecutive tamoxifen doses five days prior to IAV inoculation, with tissue harvest performed at 7 and 21DP-IAV (Fig. 4E). Immunofluorescence microscopy with quantification of *Myc*-mRNA coverage confirmed efficient epithelial *Myc* deletion (Fig. 4F,G). Phenotypically, *Krt5*^{creER};*Myc* mutants mirrored heterozygous controls in acute morbidity, incurring ~20% weight loss at 7DP-IAV (Fig. S2D).

To determine whether *Myc* deletion impacted viral replication and/or clearance, we assessed *IAV* transcript localization during the reparative phase. At 7DP-IAV, both control and *Krt5*^{creER};*Myc* mutants exhibited similar levels of epithelial *IAV*-mRNA enrichment, and by 10DP-IAV, viral transcripts were undetectable in both groups, indicating normal viral replication and clearance (Fig. 4H; Fig. S2E).

Given the role of *Myc* in cell cycle regulation,[23,25] we next evaluated epithelial proliferation and apoptosis using EdU incorporation and TUNEL staining at 7DP-IAV. Homeostatic epithelia showed no differences in EdU or TUNEL positivity between control and mutant mice (Fig. 4I-K). However, following IAV injury, *Krt5*^{creER};*Myc* mutants exhibited a marked reduction in epithelial cell proliferation compared to infected controls, while apoptosis levels remained unchanged (Fig. 4I-K). These findings indicate that *Myc* drives mitogenic surge selectively upon injury,

decoupling it from homeostatic turnover, apoptosis, or antiviral orchestration.

Anticipating chronic sequelae from blunted epithelial expansion, we scrutinized 21DP-IAV histology, yet discerned similar cell abundance and no overt dysmorphia in mutants versus controls, irrespective of IAV status (Fig. S3A,B). Given that all upper airway epithelial lineages originate from KRT5^{+} progenitors (Fig. S2F), we next examined lineage-defined cell types in *Krt5^{creER};Myc* mutants compared to infected controls to assess sustained architectural repair at 21DP-IAV. In mutant epithelium, we observed trends toward reduced KRT14^{+} basal cells, modest expansion of KRT13^{+} hillock cells, and a decrease in acetylated-tubulin^{+} ciliated cells, although none of these changes reached statistical significance (Fig. 4L; Fig. S3B). Notably, we identified a significant reduction in SCGB1A1^{+} club cells in injured mutants, accompanied by disrupted ciliated and club cell distribution at 21DP-IAV (Fig. 4L; Fig. S3B). Collectively, our data indicate that *Myc* acts as a critical injury-induced regulator of basal progenitor function, coordinating both epithelial expansion and lineage specification. Loss of *Myc* blunts proliferation and disrupts differentiation trajectories, resulting in mispatterned epithelial remodeling at 21DP-IAV.

Epithelial-Immune Crosstalk Establishes a MYC-Dependent Cxcl10–Cxcr3 Axis Driving CD8^{+} NKT-like Cell Recruitment Post-IAV. Epithelial cells, as primary targets of IAV-mediated cytopathy, orchestrate immune recruitment via secreted mediators to expedite viral clearance and mucosal restoration.[5,6] To test the hypothesis that *Myc* expression in basal cells modulates immune recruitment, we examined differentially expressed genes in our scRNA-seq dataset, focusing on IAV-enriched epithelial cells. *Cxcl10* emerged as the singular chemokine significantly upregulated, with *Myc*+ co-expression confined to the injury-responsive basal population (Fig. 5A; Fig. S3C), positioning it as a candidate for coordinating immune influx.

To map epithelial-immune communication, we applied CellChat to infer ligand-receptor interactions.[26] *Cxcl10* transcripts were detected across epithelial (serous-ductal, IAV-enriched, basal-myoepithelial) and immune (TR-macrophage, neutrophil) populations, yet its receptor, *Cxcr3*, was exclusively expressed in our CD8^{+} NKT cells (Fig. 5B-D). Probabilistic signaling analysis underscored the *Cxcl10–Cxcr3* axis as the predominant conduit linking IAV-enriched epithelia to CD8^{+} NKT cells (Fig. 5C,D), implicating this pathway in precise immune recruitment during repair. In contrast, interrogation of the *Cxcl2–Cxcr2* axis—previously tied to neutrophil dynamics[21]—revealed no epithelial *Cxcl2* expression at 7DP-IAV, excluding its role in epithelial-driven responses at this stage (Fig. 5C).

To interrogate the functional control exerted by *Myc* over this epithelial–immune chemokine axis, we profiled immune recruitment dynamics in *Krt5^{creER};Myc* mutants versus heterozygous controls at acute 7DP-IAV and convalescent 21DP-IAV phases (Fig. 5E). *In situ* hybridization disclosed a profound depletion of *Cxcl10*-mRNA across the pseudostratified airway mucosa in mutants relative to controls specifically at the acute 7DP-IAV stage (Fig. 5F–H), underscoring the requisite role of *Myc* in injury-induced chemokine induction. This blunted CXCL10 gradient translated to impaired mucosal immunity whereby mutants displayed significantly reduced CD45+ leukocyte and CD3+ T-cell infiltration at 7DP-IAV (Fig. 5H,I; Fig. S3D), with trends toward persistence at 21DP-IAV that fell short of statistical significance. Although overall CD3+ accrual normalized by 21DP-IAV, epithelial expression of hallmark CD8+ NKT effector genes—*Gzmb* and *Ccl5*—was durably subdued in mutants (Fig. 5H,J). Notably, *Gzmb*

transcripts exhibited sustained, statistically significant attenuation at 21DP-IAV (Fig. 5H,J), implying that *Myc* orchestrates not only initial recruitment but also the long-term priming and cytotoxic arming of intraepithelial effectors. Collectively, these findings establish that *Myc* orchestrates a *Cxcl10*–*Cxcr3*–dependent epithelial–immune signaling circuit, enabling selective recruitment and functional maturation of CD8$^+$ NKT cells for coordinated mucosal repair following IAV injury.

Discussion

Viral infections in the airway play a pivotal role in modulating host immune responses, influencing both the resolution of infection and the preservation of epithelial integrity essential for airway health and function. Here, we define a MYC-dependent epithelial–immune circuit that orchestrates repair of the upper respiratory tract after IAV injury. Using spatial mapping, scRNA-seq, and conditional genetics, we show that IAV targets regionally specialized epithelial lineages and elicits a MYC-driven basal progenitor response that is coupled to recruitment of cytotoxic CD8$^+$ NKT effector cells via a CXCL10–CXCR3 axis. Basal cell–specific *Myc* deletion uncouples these processes such that viral replication/clearance and gross architecture are preserved, but injury-induced proliferation, lineage allocation, and cytotoxic T cell recruitment are attenuated, resulting in subtle yet mispatterned remodeling of secretory and ciliated compartments.

Our findings extend a growing literature positioning *Myc* as a central regulator of epithelial regeneration beyond its canonical oncogenic role.[24,25,27,28] *Myc* has been implicated in coordinating proliferation and metabolic rewiring in diverse regenerative contexts, including intestinal, hepatic, and skeletal tissues.[29-31] In the lung, *c-Myc* promotes activation of the peribronchiolar smooth muscle cell niche and *Fgf10* expression after naphthalene injury, and its deletion in this compartment attenuates epithelial repair.[32] Work in corneal epithelium further demonstrates *c-Myc* maintains epithelial architecture at homeostasis and governs the balance among stratification, differentiation, and exfoliation during wound repair, in part through modulation of *p63*-dependent cell-fate programs.[25] Our data add a complementary layer by showing that, in the upper respiratory tract, *Myc* is selectively induced in KRT5$^+$ basal progenitors of pseudostratified epithelia after viral injury and is required for a full proliferative burst and appropriate differentiation into club and ciliated lineages. Across epithelial organs, *c-Myc* thus emerges as a conserved coordinator of injury-induced regeneration whose precise regulation is essential for maintaining tissue homeostasis. Whether this program is conserved across non-viral airway challenges such as chemical/environmental irritants and bacterial infection remains to be determined. In homeostatic conditions, basal cells of the stratified squamous laryngeal epithelium displayed robust *Myc* expression; nonetheless, this region experienced negligible viral insult, precluding any detectable MYC-mediated repair program. Accordingly, we propose that similar MYC-regulated programs exist in this niche but are engaged only after substantial epithelial compromise.

A key feature of our model is the integration of the MYC-driven basal progenitor program with localized cytotoxic immunity. We identify a persistent intraepithelial CD3$^+$ T cell population at 21DP-IAV, exhibiting a tissue-resident, CD8$^+$ NKT cytotoxic transcriptional signature. scRNA-seq and CellChat analysis revealed that *Myc*$^+$ basal and IAV-enriched epithelial cells are major sources of the chemokine *Cxcl10*, whereas its receptor *Cxcr3* is largely confined to these CD8$^+$ NKT cells, positioning this axis as a dominant conduit of epithelial–immune crosstalk. The CXCL10–CXCR3

axis is well recognized for directing effector T-cell trafficking to injured tissues.[33-38] In influenza models, CXCR3$^+$ CD8$^+$ T cells and lung tissue-resident memory (T_{RM}) cells provide rapid heterosubtypic protection upon re-exposure, yet subsets of CXCR3$^+$ or T_{RM} CD8$^+$ T cells can also exacerbate chronic lung pathology without significantly altering viral clearance, indicating that functional outcomes are context dependent.[35] Consistent with this complexity, *Myc*-deficient airways show reduced epithelial *Cxcl10* expression and diminished early CD3$^+$ recruitment, indicating that MYC tunes both the magnitude and positioning of cytotoxic cells during repair.

Several caveats warrant careful consideration when interpreting our results. First, our identification of a CXCR3$^+$ CD8$^+$ NKT-like population does not resolve its full heterogeneity. CXCR3 marks diverse effector subsets—including Th1-biased CD4$^+$ T cells, canonical CD8$^+$ T_{RM}, type I/II NKT cells, MAIT cells, γδ T cells, and FOXP3$^+$ regulatory T cells—each of which may respond differently to epithelial *Cxcl10* and exert distinct tissue-level effects.[37-40] Second, the functional implications of sustaining these cytotoxic cells within the upper airway epithelium remain uncertain. Their transcriptional profile, defined by residency markers (*Itga1*/CD49a*)* and effector genes (*Gzma, Gzmb, Ccl5*), suggests they are primed memory-like cells capable of rapid antiviral defense. Indeed, emerging evidence positions CD49a as a compartmental discriminator for CD8$^+$ T_{RM} cells in barrier tissues like skin, where it underpins rapid effector deployment (*Gzma, Gzmb, Ccl5, Nkg7, Cxcr3*) upon restimulation.[39] By extension, our cells may afford protective immunosurveillance against reinfection, aligning with canonical T_{RM} benefits in respiratory models.[39,40] However, their persistence may also potentiate maladaptive inflammation during recurrent insults. Distinguishing protective versus pathogenic roles will require studies incorporating lineage tracing, targeted depletion, cytokine blockade, and secondary-challenge paradigms.

These interpretive nuances extend to broader methodological constraints that shape our conclusions. For instance, we examined a single IAV strain and dose in young adult mice, leaving open questions about how aging, viral variants, or comorbidities (e.g., asthma or reflux) might reshape the MYC–CXCL10–CD8$^+$ NKT pathway. Our conditional *Myc* knockout targeted KRT5$^+$ basal cells broadly, without separating rare stem-like pools (e.g., KRT14$^+$) from more differentiated ones, nor does it address potential compensation by other *Myc* paralogs over longer time scales. Moreover, although our analyses capture structural and molecular outcomes, they do not assess physiological consequences such as mucociliary clearance, airway biomechanics, or vagal reflex function.

Despite these limitations, our findings offer compelling clinical insights, revealing how a single viral hit can leave a lasting mark on airway tissue structure and local immune defenses. This mechanism is especially relevant to post-viral vagal neuropathy, chronic cough, voice loss (dysphonia), and related unexplained problems with laryngeal sensation and movement. In such conditions, an exaggerated or poorly resolved T_{RM}-like response in the laryngeal mucosa may sustain low-grade inflammation, skew epithelial differentiation, and perturb sensory circuits, thereby prolonging symptoms despite virologic recovery. Fundamentally, our results frame airway basal cells as key hubs linking repair to immune tuning, wherein MYC-driven proliferation and chemotactic cues (such as CXCL10-mediated immune influx) orchestrate balance between adaptive memory and maladaptive persistence.
To extend these findings, future studies should determine how repeated or mixed viral exposures recalibrate this epithelial–immune circuit and

clarify when MYC-driven repair and CXCL10–CXCR3–mediated CD8+ NKT recruitment promote resilience versus precipitate maladaptive remodeling. Longitudinal approaches that integrate epithelial and immune profiling with direct assessments of neuroimmune function—such as vagal afferent activity, cough and laryngeal reflex sensitivity, and sensory nerve morphology—will be essential for establishing whether sustained cytotoxic surveillance disrupts sensory pathways in a manner that parallels human post-viral disease. In summary, our study spotlights basal *Myc* as a trigger for injury-timed control of epithelial growth, cell fate decisions, and chemokine-summoned influx of cytotoxic CD8+ NKT cells across the upper respiratory tract. This coordinated program likely contributes to efficient viral control and the establishment of local memory, but may also set the stage for persistent epithelial remodeling and neuroimmune dysregulation when dysbalanced.

Methods

Animals

All experimental procedures were performed in the American Association for Accreditation of Laboratory Animal Care (AAALAC)-certified laboratory animal facility at the University of California, San Diego (UCSD). All animal husbandry and experiments were conducted under approved Institutional Animal Care and Use Committee (IACUC) guidelines. Wild-type C57BL/6 (JAX 000664), *Krt5*^{CreERT2} (JAX 029155), *Ascl1*^{CreERT2} (JAX 012882), and *Rosa*$^{lxl\text{-}tdTomato}$ (*Ai14*, JAX 007914) lines were purchased from the Jackson lab. *Myc-flox* (MMRRC 036778) line was gifted from Rob Signer at UCSD. All the *cre* lines we used in this study were kept in C57BL/6 background. All *cre* driver lines in heterozygous form are viable and fertile, and no abnormal phenotypes were detected. Both male and female mice were used in the experiment. Adult mice were 8-12 weeks of age for all experiments. The experiments were not randomized, and the investigators were not blinded to allocation during experiments and outcome assessment.

Influenza A virus (IAV) infection

Influenza strain A/H1N1/PR/8 strain was obtained from ATCC (VR-95PQ). Briefly, mice were anesthetized with 3.5% isoflurane for 15 min until bradypnea was observed. Virus dissolved in 35 µl of PBS was pipetted onto the nostrils of anesthetized mice, whereupon they aspirated the fluid directly into their airways. Control and experimental groups were infected simultaneously in the same cohort by the same investigator so that direct comparison between groups was justified and appropriate.

Tissue collection and immunofluorescence

Mice were euthanized by CO2 inhalation followed by transcardial perfusion with PBS to remove circulating blood. The larynx-trachea was isolated and fixed overnight in 1%PFA or immediately embedded in OCT, flash frozen using 2-Methylbutane and liquid nitrogen and stored at –80°C. Using a cryostat, the larynx-trachea was then sectioned (12 µm) and stored at –20°C. Unfixed/lightly fixed tissue was then washed in PBS for 5mins to remove OCT, heated to boiling in 10 mM citrate buffer (pH 9) for antigen retrieval and treated with 0.5% Triton X-100 in PBS for 15mins. All sections were processed for immunostaining following a standard protocol.[41] *Ascl1* and *Krt5* recombination was induced via Tamoxifen IP administration with dose of 100mg/kg for either two or three consecutive days. All primary and secondary antibodies used are listed in TableS2. Primary antibodies were applied overnight at 4°C, while secondary antibodies were applied for 1hr at room temperature. Sections were incubated with DAPI (1:1000 ratio) for 10 min at RT. Slides were mounted and coverslipped with Prolong Diamond mounting media (Fisher P36970), cured flat at room temperature in the dark for 24 h, and stored at 4°C. Each experiment was replicated at least twice for all timepoints and targets assessed.

Tissue processing and cell sorting

Whole upper airway (larynx-trachea) was mechanically dissociated by mincing tissue with razor blades in solution containing 5 ml of RPMI 1640 (Thermo Scientific) with 10% fetal bovine serum, 1 mM HEPES (Life Technology), 1 mM $MgCl_2$ (Life Technology), 1 mM $CaCl_2$ (Sigma), 0.5 mg ml^{-1} collagenase D and type I/Dispase (Roche), and 0.25 mg DNase I (Roche). Minced tissue was then digested by shaking at around 150 rpm

for 30 min at 37 °C. Following incubation, upper airway pieces were mechanically dissociated further by straining through a MACS 70 μm filter. Red blood cells were removed by the addition of 1 ml of RBC lysis buffer (BioLegend) to each tube and incubation at room temperature for 1 min. Single-cell suspensions were pelleted (1,500 rpm, 4 °C, 5 min) and stained with Fc blocking antibody (5 mg ml^{-1}, BD). For FACS, the following antibodies were used: (Immune) 1:1000 BV510-conjugated anti-CD45 (BioLegend, no. 103138), (Epithelial) 1:1000 APC-FITC-conjugated anti-Epcam (BioLegend, no. 118214), and (Endothelial) 1:1000 PE-conjugated anti-CD31 (BioLegend, no. 102508). Cells were then stained using live/dead dye (CD11b: Brilliant Violet 450, BioLegend, no. 75-0112-U025) before being resuspended in 2% FBS + 1:2000 DAPI. All FACS sorting for scRNA-seq library preparation was done on a BD FACSAria Fusion Sorter (BD Biosciences) analyzer with three lasers (405, 488 and 640 nm) at the Flow Cytometry Core at VA San Diego Health Care System.

Bulk RNA-seq and data analysis

Total RNA from 10wk old adult WT upper airway (larynx/trachea) tissue was extracted as described above. cDNA libraries were constructed using Illumina TruSeq RNA Library Prep Kit V2 (Illumina) and sequenced on the HiSeq4000 platform (Illumina) at the Institute for Genomic Medicine (IGM) at UCSD. FASTQ files were aligned to the mouse reference genome (mm10) by using Bowtie2[42] with default settings. Differential gene expression analysis was performed using Cufflinks.[43] P-values were adjusted by the Benjamini-Hochberg method to control False Discovery Rate (FDR) at 0.05. Heatmaps and volcano plots were generated by ggplot2 (version 3.3.2) using RStudio. (v. 2024.04.0 Build 735) running R 4.3.3 (R Core Team). Once exclusively differentially expressed genes were identified, we performed tests of enrichment using Gene Ontology (GO) annotations utilizing Enrichr (v2024)[44] as previously described.[45]

10x Chromium scRNAseq and data analysis

Single-cell RNA sequencing (scRNA-seq) was performed using the 10× Genomics Chromium platform as previously described.[10] Briefly, dissociated cell suspensions were loaded onto the Chromium Controller to generate single-cell gel bead emulsions, followed by cDNA synthesis and library preparation using the Chromium Single Cell 3′v3 kit (10X Genomics, Pleasanton, CA). Libraries were sequenced on an Illumina NovaSeq 6000, and raw reads were processed with Cell Ranger (v3.0.2, 10× Genomics) using the mouse reference genome (GRCm38) to generate single-cell gene barcode matrices. Influenza A Virus complete gene sequence was imputed into the reference genome for *in silico* transcript identification (TableS1). Downstream analyses—including quality control, normalization, clustering, and differential expression—were performed in Seurat (v4.0.5)[46,47] following the previously mentioned computational workflow.[10] Unless otherwise noted, identical parameters and filtering thresholds were applied. To account for technical and biological covariates, cell cycle phase scores (S and G2/M), mitochondrial transcript percentage, and gene feature counts (nFeature_RNA) were incorporated into the dataset and regressed during data scaling to minimize their confounding effects on clustering.

To infer and quantify cell–cell signaling, we applied the CellChat R package (v1.x) to the processed single-cell transcriptomic data. Ligand–receptor interactions and their associated cofactors were evaluated using the curated CellChatDB database (mouse version, ~2,021 validated interactions).[26] Communication networks were represented as directed, weighted graphs, and visualized using hierarchical plots, circle plots, bubble plots, and chord diagrams. Centrality metrics (e.g. in-degree, out-degree, betweenness) were computed to determine dominant signaling sources, targets, and mediators. Pattern recognition and manifold learning approaches were applied to identify global communication patterns and context-specific signaling differences across conditions.

To assess pathway-level activity across our IAV-enriched epithelial subpopulations, we applied the irGSEA R package (v2.1.5) for rank-based, single-cell gene set enrichment analysis.[48] Gene sets were derived from MSigDB (Hallmark and KEGG collections) (version 7.4.1). Normalized expression matrices from Seurat objects were imported into irGSEA, and enrichment scores were calculated using the AUCell (version 1.14.0), UCell (version 1.1.0), singscore (version 1.12.0), GSVA (version 1.40.1) and Viper (version 1.32.0) algorithms implemented within the package. Scores were computed on a per-cell basis and summarized by cell type and

condition. Differential pathway enrichment was visualized as violin and dot plots to highlight compartment-specific activation patterns. All parameters followed default settings in irGSEA unless otherwise specified.

Cellular lineage and differentiation trajectories were reconstructed using Monocle3 (1.4.26) to infer dynamic transcriptional transitions within epithelial IAV-enriched subpopulations.[49] Briefly, Seurat-processed data were converted to a *cell_data_set* object using the *as.cell_data_set()* function, retaining normalized expression values and annotated metadata. Dimensionality reduction was performed using UMAP and PCA embeddings previously generated in Seurat. Cells were ordered in pseudotime using *learn_graph()* and *order_cells(),* with root nodes defined by basal populations. Pseudotime-associated genes were identified using *graph_test(),* and trajectory-dependent gene expression patterns were visualized using *plot_cells()* functions. Default Monocle3 parameters were used unless otherwise noted.

RNAscope in situ hybridization

All staining procedures were performed using the RNAscope Fluorescent Multiplex Kit V2 (Advanced Cell Diagnostics, no. 323100) following the manufacturer's instructions. The following probes from Advanced Cell Diagnostics were used: Mm-*IAV* (no. 521181), Mm-*Myc* (no. 413451), Mm-*Cxcl10* (no. 408921), Mm-*tdTomato* (no. 317041), Mm-*Gzmb* (no. 490191), Mm-*Ccl5* (no. 469601).

Cell proliferation and apoptosis

Cell proliferation was assessed using the Click-iT™ EdU Cell Proliferation Kit (C10337, Invitrogen), which detects DNA synthesis through copper-catalyzed azide–alkyne cycloaddition between incorporated 5-ethynyl-2′-deoxyuridine (EdU) and a fluorescent azide probe. Adult mice received 1 mL of a 400 μM EdU solution (Invitrogen, diluted in PBS) by intraperitoneal injection, and upper airway tissues were collected 1 hour later. Samples were fixed in 1% paraformaldehyde (PFA) overnight at 4°C, washed in PBS for 30 minutes, and embedded in OCT before cryosectioning and EdU detection according to the manufacturer's protocol.

Apoptosis was measured using the Click-iT™ Plus TUNEL Assay (C10245, Invitrogen), which labels DNA strand breaks via terminal deoxynucleotidyl transferase (TdT)–mediated incorporation of alkyne-modified nucleotides, followed by fluorescent azide detection using the same click-chemistry–based reaction. Tissue preparation, fixation, and embedding were identical to those described for EdU staining, and TUNEL labeling was performed following the manufacturer's instructions.

Lineage tracing

Tamoxifen dissolved in corn oil was administered via intraperitoneal injection at 25 mg/kg once daily for three consecutive days.

Cell count quantification

All cell counts and area measurements were quantified at 20× magnification from 3–4 whole-mount coronal images spanning the pharyngolaryngeal-to-tracheobronchial axis (Fig. S1B). Images were analyzed using an automated pipeline in QuPath (v0.6.0). Briefly, the epithelium was manually annotated as a region of interest (ROI) and subdivided into regional compartments, including tracheal surface epithelium (SE), subglottic SE, supraglottic SE, and submucosal glands (SMG). For marker-positive cell counts or total feature area (μm²), the QuPath *create_threshold* function was applied within each annotated epithelial ROI to accurately label the target signal. The *cell_detection* function was then used within the same ROI to identify $DAPI^+$ nuclei and determine total cell numbers. Threshold-defined feature counts were normalized to $DAPI^+$ counts to calculate the percentage of positive cells; alternatively, threshold-defined feature area was recorded within each ROI and reported as total area (μm²) or expressed in arbitrary units (AU) as indicated.

Statistics

All analyses were performed using GraphPad Prism 10. Data were first assessed for normality (Shapiro–Wilk) and homogeneity of variance (F test) to determine whether parametric or non-parametric tests were appropriate. For normally distributed data with equal variance, statistical comparisons used t-tests (two groups) or one-way/two-way ANOVA (multiple groups or multiple variables), followed by the appropriate post-hoc corrections (Dunnett's, Tukey's, or Fisher's LSD) as indicated in figure legends. When normality or variance assumptions were not met, non-parametric equivalents

were applied. Results are reported as mean ± SE, and significance was defined as $p \leq 0.05$.

Data and code availability

Bulk and single cell RNA-seq data have been deposited at the Gene Expression Omnibus (GEO) and are publicly available as of the date of publication. All data generated supporting the findings of this study are available in the manuscript. Further information is available from the lead author upon reasonable request. This paper does not report original code.

Acknowledgements

The authors thank Sun lab members for discussions. UCSD Microscopy Core was supported by NINDS-P30NS047101. This work was supported by grants NIH NHLBI R01 AT011676-01 (to X.S.), 1R01 HL160019-01 (to X.S.), NIH NIDCD F32 DC021634-01 (to A.G.F.) and ASLHF (to A.G.F.).

Author contributions

Conceptualization: A.G.F, X.S. Methodology: A.G.F. Investigation: A.G.F., L.X., B.P., N.K., J.V. Visualization: A.G.F. Funding acquisition: A.G.F., X.S. Supervision: X.S. Writing – original draft: A.G.F. Writing – review & editing: A.G.F., X.S.

Competing interests

The authors declare no competing interests.

References

1 An, R. *et al.* Single-Cell View into the Role of Microbiota Shaping Host Immunity in the Larynx. *iScience* (2024).

2 Jette, M. E., Dill-McFarland, K. A., Hanshew, A. S., Suen, G. & Thibeault, S. L. The human laryngeal microbiome: effects of cigarette smoke and reflux. *Sci Rep* **6**, 35882 (2016). https://doi.org/10.1038/srep35882

3 Thibeault, S. L., Rees, L., Pazmany, L. & Birchall, M. A. At the crossroads: mucosal immunology of the larynx. *Mucosal Immunol* **2**, 122-128 (2009). https://doi.org/10.1038/mi.2008.82

4 Niec, R. E., Rudensky, A. Y. & Fuchs, E. Inflammatory adaptation in barrier tissues. *Cell* **184**, 3361-3375 (2021). https://doi.org/10.1016/j.cell.2021.05.036

5 Hewitt, R. J. & Lloyd, C. M. Regulation of immune responses by the airway epithelial cell landscape. *Nat Rev Immunol* **21**, 347-362 (2021). https://doi.org/10.1038/s41577-020-00477-9

6 Yang, J. & Yan, H. Mucosal epithelial cells: the initial sentinels and responders controlling and regulating immune responses to viral infections. *Cell Mol Immunol* **18**, 1628-1630 (2021). https://doi.org/10.1038/s41423-021-00650-7

7 Chen, X. *et al.* Host Immune Response to Influenza A Virus Infection. *Front Immunol* **9**, 320 (2018). https://doi.org/10.3389/fimmu.2018.00320

8 King, R. E. *et al.* A Novel In Vivo Model of Laryngeal Papillomavirus-Associated Disease Using Mus musculus Papillomavirus. *Viruses* **14** (2022). https://doi.org/10.3390/v14051000

9 King, R. E. *et al.* The Larynx is Protected from Secondary and Vertical Papillomavirus Infection in Immunocompetent Mice. *The Laryngoscope* (2023).

10 Foote, A. G. & Sun, X. Cellular Heterogeneity and Patterning Strategies as Revealed by Upper Respiratory Epithelium Single Cell Atlas. *iScience*, 112845 (2025).

11 Jin, X. *et al.* Global burden of upper respiratory infections in 204 countries and territories, from 1990 to 2019. *EClinicalMedicine* **37**, 100986 (2021). https://doi.org/10.1016/j.eclinm.2021.100986

12 Lee, B. & Woo, P. Chronic cough as a sign of laryngeal sensory neuropathy: diagnosis and treatment. *Annals of Otology, Rhinology & Laryngology* **114**, 253-257 (2005).

13 Rees, C. J., Henderson, A. H. & Belafsky, P. C. Postviral vagal neuropathy. *Ann Otol Rhinol Laryngol* **118**, 247-252 (2009). https://doi.org/10.1177/000348940911800402

14 Garcia-Vicente, P. *et al.* Chronic cough in post-COVID syndrome: Laryngeal electromyography findings in vagus nerve neuropathy. *PLoS One* **18**, e0283758 (2023). https://doi.org/10.1371/journal.pone.0283758

15 Amin, M. R. & Koufman, J. A. Vagal neuropathy after upper respiratory infection: a viral etiology? *Am J Otolaryngol* **22**, 251-256 (2001). https://doi.org/10.1053/ajot.2001.24823

16 Jeyakumar, A., Brickman, T. M. & Haben, M. Effectiveness of amitriptyline versus cough suppressants in the treatment of chronic cough resulting from postviral vagal neuropathy. *Laryngoscope* **116**, 2108-2112 (2006). https://doi.org/10.1097/01.mlg.0000244377.60334.e3

17 Bhatt, N. K., Pipkorn, P. & Paniello, R. C. Association between upper respiratory infection and idiopathic unilateral vocal fold paralysis. *Annals of Otology, Rhinology & Laryngology* **127**, 667-671 (2018).

18 Wang, W. *et al.* Stress keratin 17 enhances papillomavirus infection-induced disease by downregulating T cell recruitment. *PLoS Pathog* **16**, e1008206 (2020). https://doi.org/10.1371/journal.ppat.1008206

19 Smith, A. M. & Perelson, A. S. Influenza A virus infection kinetics: quantitative data and models. *Wiley Interdiscip Rev Syst Biol Med* **3**, 429-445 (2011). https://doi.org/10.1002/wsbm.129

20 Bin, N. R. *et al.* An airway-to-brain sensory pathway mediates influenza-induced sickness. *Nature* (2023). https://doi.org/10.1038/s41586-023-05796-0

21 Rudd, J. M. *et al.* Neutrophils Induce a Novel Chemokine Receptors Repertoire During Influenza Pneumonia. *Front Cell Infect Microbiol* **9**, 108 (2019). https://doi.org/10.3389/fcimb.2019.00108

22 Krenz, B., Lee, J., Kannan, T. & Eilers, M. Immune evasion: An imperative and consequence of MYC deregulation. *Mol Oncol* **18**, 2338-2355 (2024). https://doi.org/10.1002/1878-0261.13695

23 Pelengaris, S. & Khan, M. The many faces of c-MYC. *Arch Biochem Biophys* **416**, 129-136 (2003). https://doi.org/10.1016/s0003-9861(03)00294-7

24 Dhanasekaran, R. *et al.* The MYC oncogene—the grand orchestrator of cancer growth and immune evasion. *Nature reviews Clinical oncology* **19**, 23-36 (2022).

25 Portal, C., Wang, Z., Scott, D. K., Wolosin, J. M. & Iomini, C. The c-Myc oncogene maintains corneal epithelial architecture at homeostasis, modulates p63 expression, and enhances proliferation during tissue repair. *Invest Ophth Vis Sci* **63**, 3-3 (2022).

26 Jin, S. *et al.* Inference and analysis of cell-cell communication using CellChat. *Nat Commun* **12**, 1088 (2021). https://doi.org/10.1038/s41467-021-21246-9

27 Zanet, J. *et al.* Endogenous Myc controls mammalian epidermal cell size, hyperproliferation, endoreplication and stem cell amplification. *J Cell Sci* **118**, 1693-1704 (2005). https://doi.org/10.1242/jcs.02298

28 Madden, S. K., de Araujo, A. D., Gerhardt, M., Fairlie, D. P. & Mason, J. M. Taking the Myc out of cancer: toward therapeutic strategies to directly inhibit c-Myc. *Mol Cancer* **20**, 3 (2021). https://doi.org/10.1186/s12943-020-01291-6

29 Luo, W. *et al.* c-Myc inhibits myoblast differentiation and promotes myoblast proliferation and muscle fibre hypertrophy by regulating the expression of its target genes, miRNAs and lincRNAs. *Cell Death Differ* **26**, 426-442 (2019). https://doi.org/10.1038/s41418-018-0129-0

30 Purhonen, J., Klefstrom, J. & Kallijarvi, J. MYC-an emerging player in mitochondrial diseases. *Front Cell Dev Biol* **11**, 1257651 (2023). https://doi.org/10.3389/fcell.2023.1257651

31 Qu, A. *et al.* Role of Myc in hepatocellular proliferation and hepatocarcinogenesis. *J Hepatol* **60**, 331-338 (2014). https://doi.org/10.1016/j.jhep.2013.09.024

32 Volckaert, T., Campbell, A. & De Langhe, S. c-Myc regulates proliferation and Fgf10 expression in airway smooth muscle after airway epithelial injury in mouse. *PLoS One* **8**, e71426 (2013). https://doi.org/10.1371/journal.pone.0071426

33 Barros, L. *et al.* CD8(+) tissue-resident memory T-cell development depends on infection-matching regulatory T-cell types. *Nat Commun* **14**, 5579 (2023). https://doi.org/10.1038/s41467-023-41364-w

34 Rubinstein, A. *et al.* CXCR3-Expressing T Cells in Infections and Autoimmunity. *Front Biosci (Landmark Ed)* **29**, 301 (2024). https://doi.org/10.31083/j.fbl2908301
35 Guo, K. *et al.* The chemokine receptor CXCR3 promotes CD8(+) T cell-dependent lung pathology during influenza pathogenesis. *Sci Adv* **10**, eadj1120 (2024). https://doi.org/10.1126/sciadv.adj1120
36 Liu, J. *et al.* Local production of the chemokines CCL5 and CXCL10 attracts CD8+ T lymphocytes into esophageal squamous cell carcinoma. *Oncotarget* **6**, 24978-24989 (2015). https://doi.org/10.18632/oncotarget.4617
37 Groom, J. R. & Luster, A. D. CXCR3 in T cell function. *Exp Cell Res* **317**, 620-631 (2011). https://doi.org/10.1016/j.yexcr.2010.12.017
38 Tokunaga, R. *et al.* CXCL9, CXCL10, CXCL11/CXCR3 axis for immune activation - A target for novel cancer therapy. *Cancer Treat Rev* **63**, 40-47 (2018). https://doi.org/10.1016/j.ctrv.2017.11.007
39 Cheuk, S. *et al.* CD49a Expression Defines Tissue-Resident CD8(+) T Cells Poised for Cytotoxic Function in Human Skin. *Immunity* **46**, 287-300 (2017). https://doi.org/10.1016/j.immuni.2017.01.009
40 Johnson, M. D., Witherden, D. A. & Havran, W. L. The Role of Tissue-resident T Cells in Stress Surveillance and Tissue Maintenance. *Cells* **9** (2020). https://doi.org/10.3390/cells9030686
41 Foote, A. G., Lungova, V. & Thibeault, S. L. Piezo1-expressing vocal fold epithelia modulate remodeling via effects on self-renewal and cytokeratin differentiation. *Cell Mol Life Sci* **79**, 591 (2022). https://doi.org/10.1007/s00018-022-04622-6
42 Langmead, B. & Salzberg, S. L. Fast gapped-read alignment with Bowtie 2. *Nat Methods* **9**, 357-359 (2012). https://doi.org/10.1038/nmeth.1923
43 Trapnell, C. *et al.* Transcript assembly and quantification by RNA-Seq reveals unannotated transcripts and isoform switching during cell differentiation. *Nat Biotechnol* **28**, 511-515 (2010). https://doi.org/10.1038/nbt.1621
44 Xie, Z. *et al.* Gene Set Knowledge Discovery with Enrichr. *Curr Protoc* **1**, e90 (2021). https://doi.org/10.1002/cpz1.90
45 Foote, A. G., Wang, Z., Kendziorski, C. & Thibeault, S. L. Tissue specific human fibroblast differential expression based on RNAsequencing analysis. *BMC Genomics* **20**, 308 (2019). https://doi.org/10.1186/s12864-019-5682-5
46 Satija, R., Farrell, J. A., Gennert, D., Schier, A. F. & Regev, A. Spatial reconstruction of single-cell gene expression data. *Nat Biotechnol* **33**, 495-502 (2015). https://doi.org/10.1038/nbt.3192
47 Becht, E. *et al.* Dimensionality reduction for visualizing single-cell data using UMAP. *Nat Biotechnol* (2018). https://doi.org/10.1038/nbt.4314
48 Fan, C. *et al.* irGSEA: the integration of single-cell rank-based gene set enrichment analysis. *Brief Bioinform* **25** (2024). https://doi.org/10.1093/bib/bbae243
49 Trapnell, C. *et al.* The dynamics and regulators of cell fate decisions are revealed by pseudotemporal ordering of single cells. *Nat Biotechnol* **32**, 381-386 (2014). https://doi.org/10.1038/nbt.2859

MAIN FIGURES

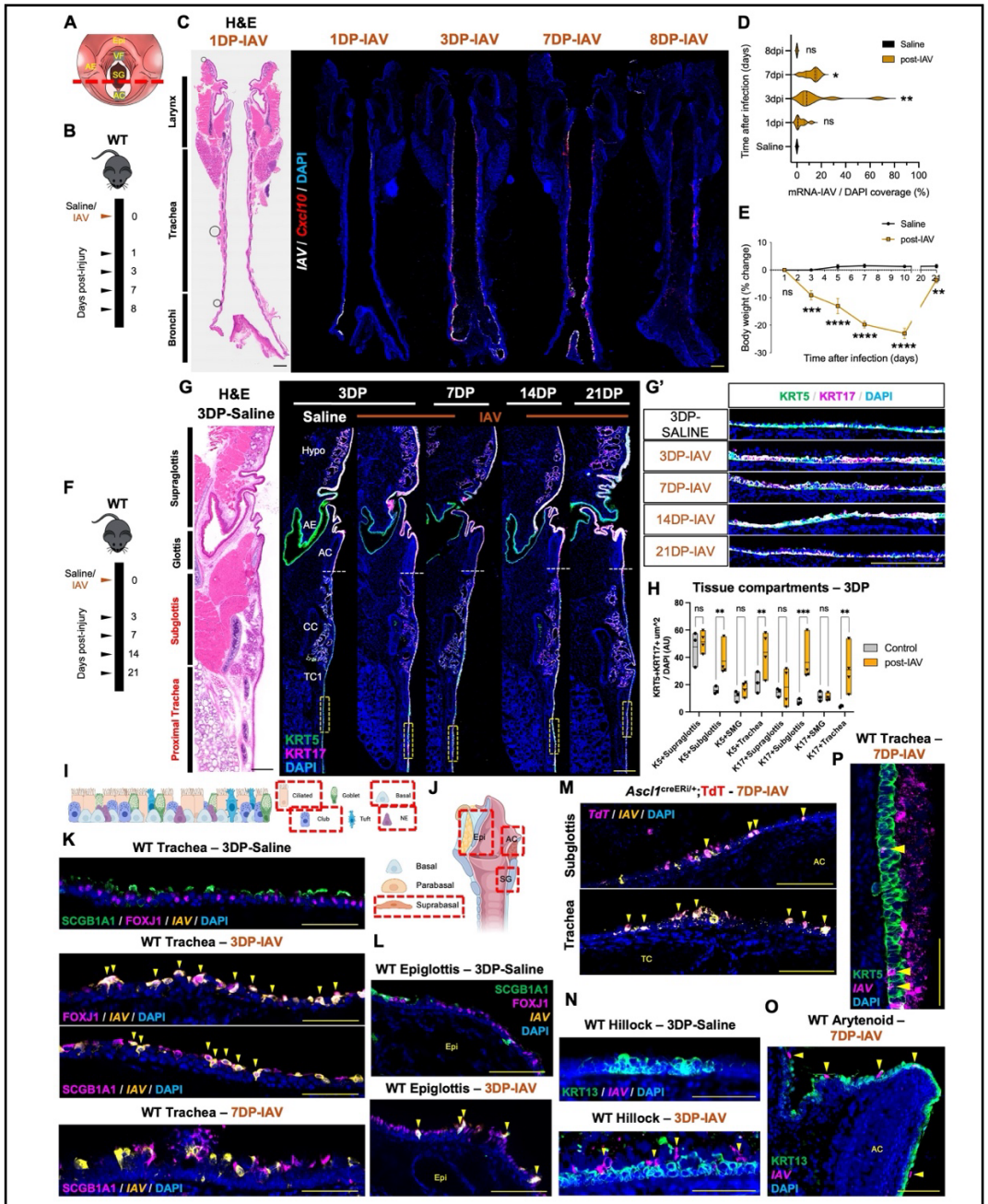

Fig 1. IAV infection induces transient epithelial injury with broad viral tropism (A,B) Schematics of upper airway coronal sectioning and IAV infection timeline. (C) H&E and RNAscope detection of IAV-mRNA (white) and Cxcl10 (red) at 1, 3, 7, and 8DP-IAV. (D) Quantification of epithelial IAV-mRNA coverage (one-way ANOVA with Dunnett's post-hoc test; mean ± SEM; n = 3/group). (E) Body weight change following infection (Welch's t-test; mean ± SEM; n = 8/group). (F) Timeline schematic corresponding to panels G–G'. (G,G') H&E and immunofluorescence for KRT5 (green) and KRT17 (magenta) showing basal cell hyperplasia at 3–14DP-IAV with resolution by 21DP-IAV; dashed boxes indicate higher-magnification insets. (H) Quantification of KRT5/KRT17 epithelial coverage across airway compartments (two-way ANOVA with Fisher's LSD post-hoc test; mean ± SEM). (I,J) Schematics highlighting epithelial diversity and airway regions enriched for IAV-mRNA. (K–P) RNAscope co-localization of IAV-mRNA with epithelial lineage markers (FOXJ1, SCGB1A1, ASCL1, KRT5, KRT13) at 3 and 7DP-IAV. DAPI, blue. Scale bars: 500 μm (C,G), 100 μm (others). *P < 0.05, **P < 0.005, ***P < 0.0005; ns, not significant.

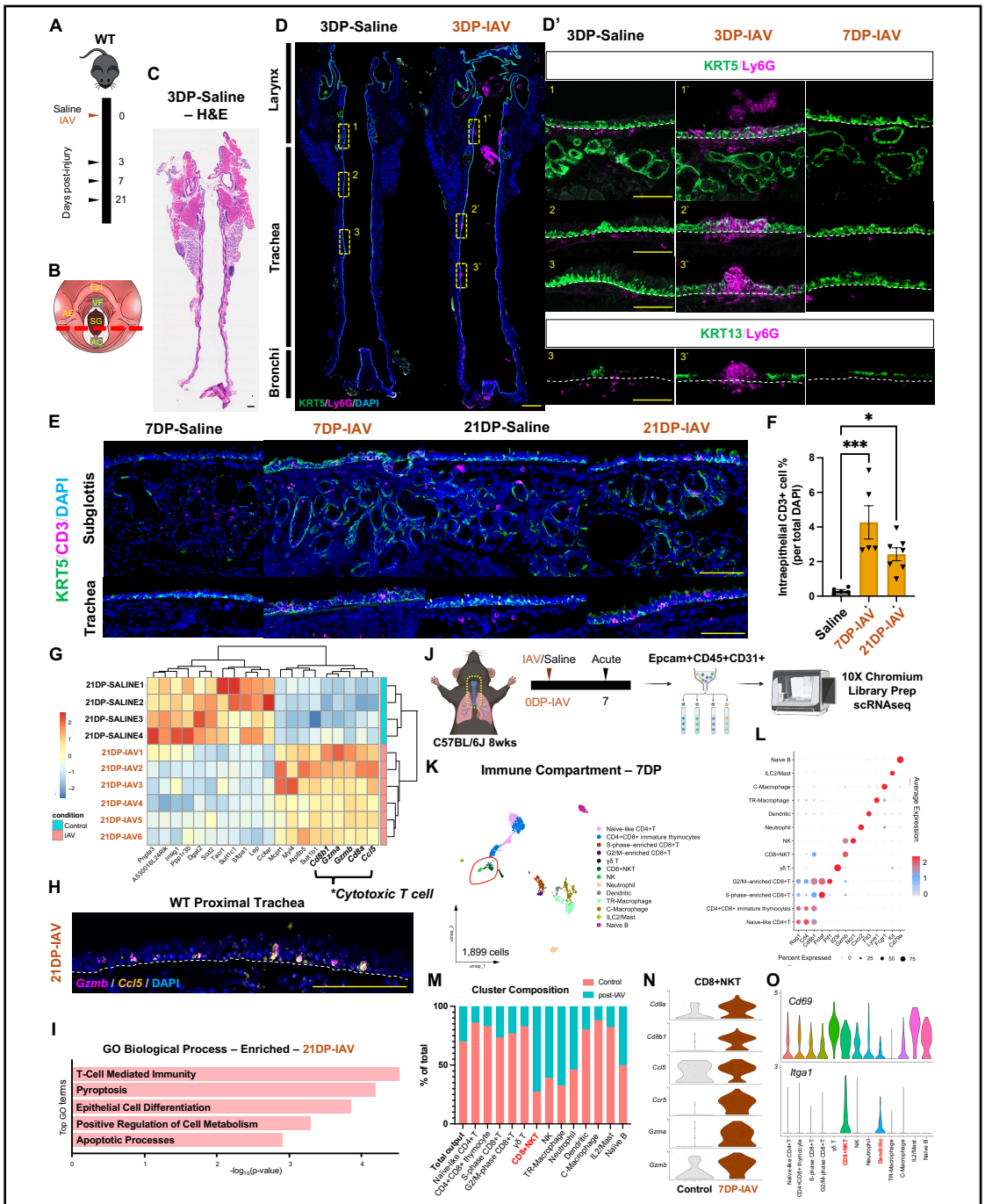

Fig 2. Acute IAV infection recruits neutrophils and establishes persistent intraepithelial CD8⁺ NKT cells. (A,B) Schematics of IAV infection timeline and airway sectioning. (C) H&E staining of sa-line-treated controls at 3 DP. (D,D′) Immunofluorescence for Ly6G⁺ neutrophils at 3 and 7 DP-IAV demonstrating epithelial infiltration; dashed boxes indicate insets. (E) Immunofluorescence showing CD3⁺ intraepithelial T cells in subglottic and tracheal epithelium at 7 DP-IAV that persist at 21 DP-IAV. (F) Quantification of CD3⁺ epithelial coverage (one-way ANOVA with Dunnett's post-hoc test; mean ± SEM). (G) Bulk RNA-seq showing increased expression of cytotoxic T-cell genes (Cd8a, Cd8b1, Ccl5, Gzma, Gzmb) at 21 DP-IAV. (H) RNAscope co-localization of Gzmb and Ccl5 transcripts at 21 DP-IAV. (I) Top enriched GO biological processes from bulk RNA-seq at 21 DP-IAV. (J) Schematic of scRNA-seq workflow. (K) UMAP of immune populations at 7 DP-IAV (n = 8 biological replicates). (L) Dot plot of top cluster markers. (M) Immune cluster composition comparing saline and IAV. (N,O) Vio-lin plots showing enrichment of cytotoxic and tissue-resident gene signatures in CD8⁺ NKT cells. DAPI, blue. Scale bars: 500 µm (C,D), 100 µm (others). *P < 0.05, **P < 0.005, ***P < 0.0005; ns, not significant.

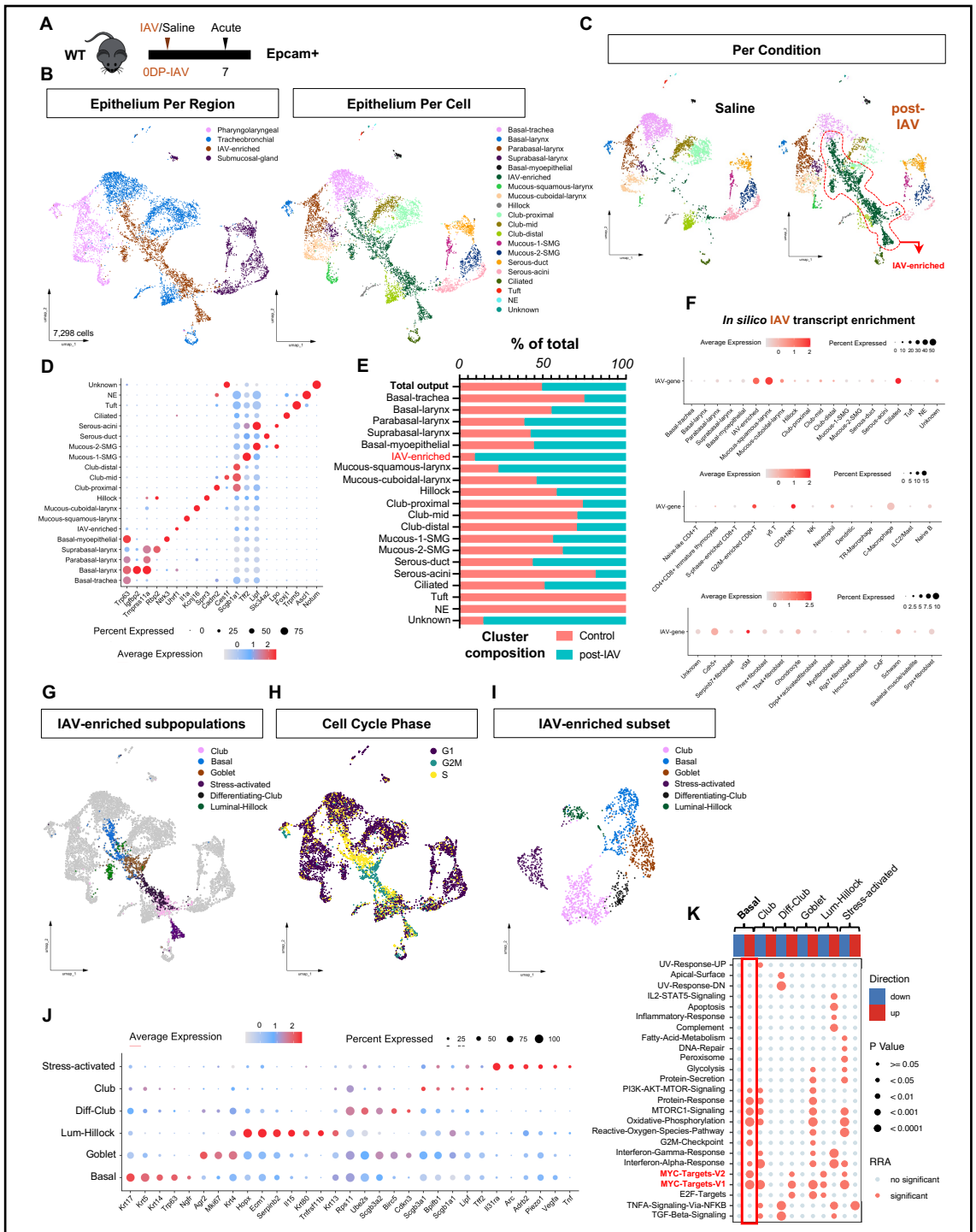

Fig 3. scRNA-seq identifies *Myc*-driven basal progenitor programs within IAV-enriched epithelial populations. (A) Schematic of scRNA-seq experimental design. (B) Integrated UMAP of upper airway epithelial populations highlighting regional and cell-type diversity. (C) UMAP colored by condition (saline vs IAV) identifying IAV-enriched epithelial clusters. (D) Dot plot of top markers defining epithelial clusters. (E) Cluster composition comparing saline and IAV conditions. (F) *In silico* viral transcript mapping demonstrating preferential IAV enrichment in epithelial lineages at 7DP-IAV. (G–I) UMAPs highlighting IAV-enriched epithelial subsets and associated cell-cycle states (G1, S, G2M). (J) Dot plot of markers defining IAV-enriched clusters. (K) Integrated regulatory GSEA identifying activation of MYC target pathways in IAV-enriched basal progenitors. WT, wild-type; DP, days post.

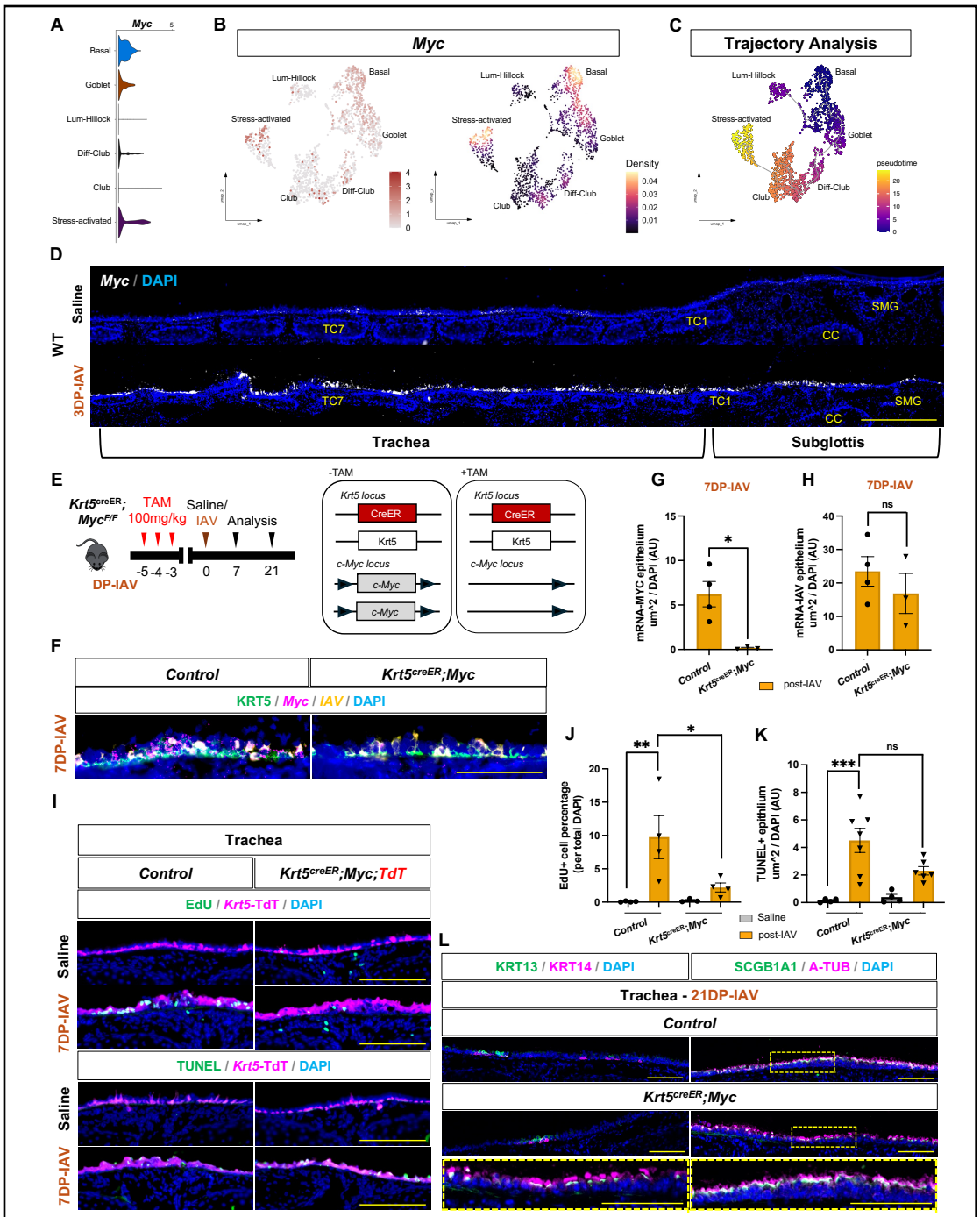

Fig 4. MYC promotes basal progenitor expansion and lineage remodeling during post-IAV epithelial repair. (A,B) Violin and feature plots showing *Myc* expression across IAV-enriched epithelial populations at 7DP-IAV. (C) Monocle3 pseudotime trajectory analysis of IAV-enriched epithelial subsets. (D) Immunofluorescence at 3DP-IAV demonstrating ectopic *Myc* expression in damaged pseudostratified epithelium. (E) Experimental schematic for basal cell–specific *Myc* deletion. (F) Immunofluorescence confirming *Myc* loss following tamoxifen induction. (G,H) Quantification of epithelial *Myc*-mRNA and *IAV*-mRNA coverage (Student's t-test; mean ± SEM). (I) EdU and TUNEL staining assessing proliferation and apoptosis at 7DP-IAV. (J,K) Quantification of proliferative and apoptotic indices (one-way ANOVA with Tukey's post-hoc test; mean ± SEM). (L) Immunofluorescence of lineage marker–positive cells in tracheal epithelium at 21DP-IAV. DAPI, blue. Scale bars: 500 µm (D), 100 µm (others). *P < 0.05, **P < 0.005, ***P < 0.0005; ns, not significant.

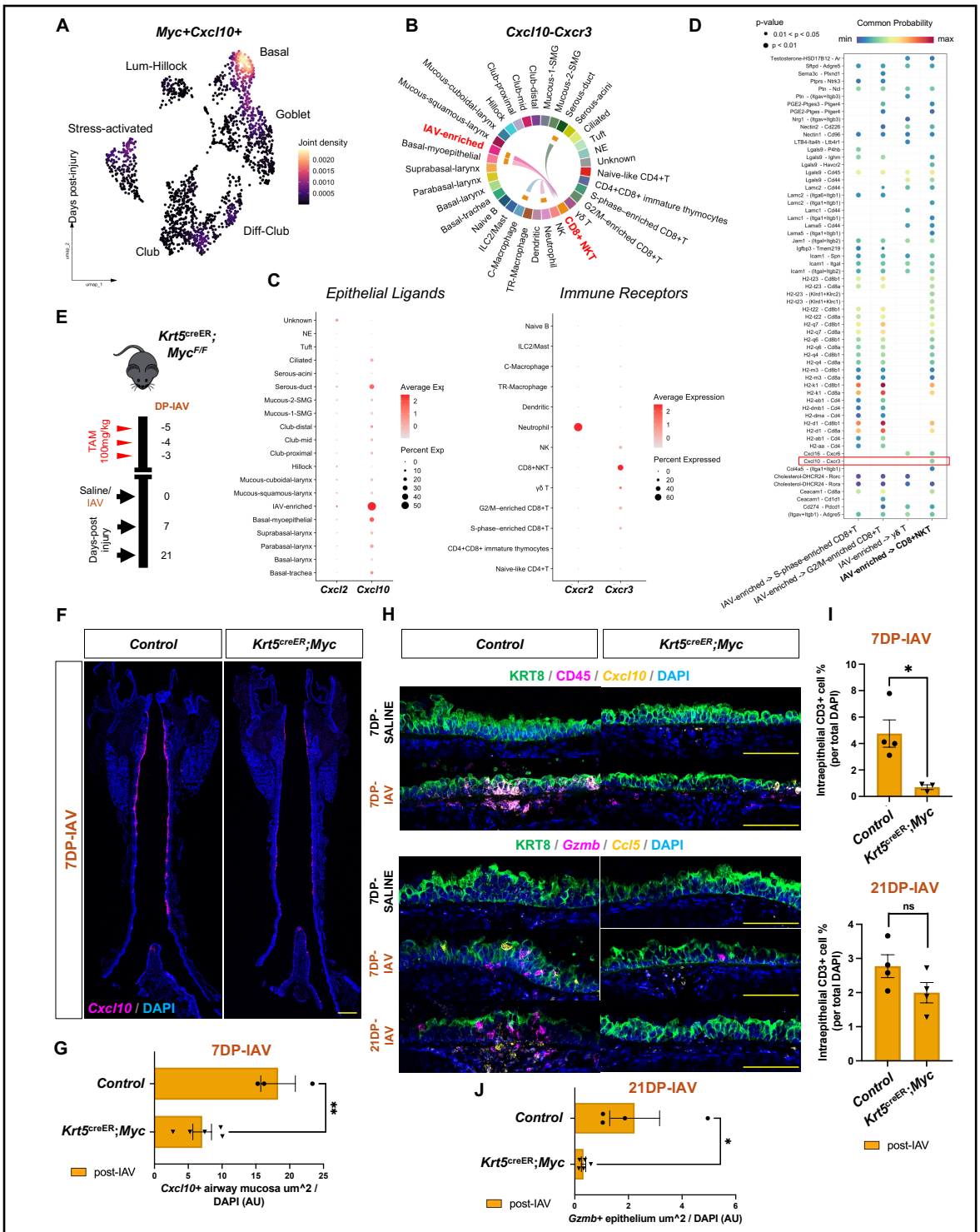

Fig 5. MYC-dependent epithelial CXCL10 signaling recruits CD8⁺ NKT cells during post-IAV repair. (A) UMAP of IAV-enriched epithelial populations showing co-expression of *Myc* and *Cxcl10* at 7DP-IAV. (B-D) CellChat analysis identifying CXCL10–CXCR3 as the dominant IAV-enriched-to-CD8⁺ NKT signaling axis. (E) Schematic of tamoxifen induction and IAV infection timeline in Krt5^{CreER};Myc mutant mice. (F,G) Whole-mount RNAscope imaging and quantification showing reduced epithelial *Cxcl10* expression in Krt5^{CreER};Myc mutants at 7DP-IAV. (H) Immunofluorescence showing reduced CD45⁺ immune infiltration and epithelial *Gzmb*/*Ccl5* expression in mutants at 7 and 21DP-IAV. (I) Quantification of intraepithelial CD3⁺ cells. (J) Quantification of epithelial *Gzmb* expression at 21DP-IAV. DAPI, blue. Scale bars: 500 µm (F), 100 µm (others). *P < 0.05, **P < 0.005, ***P < 0.0005; ns, not significant.

SUPPLEMENTAL FIGURES

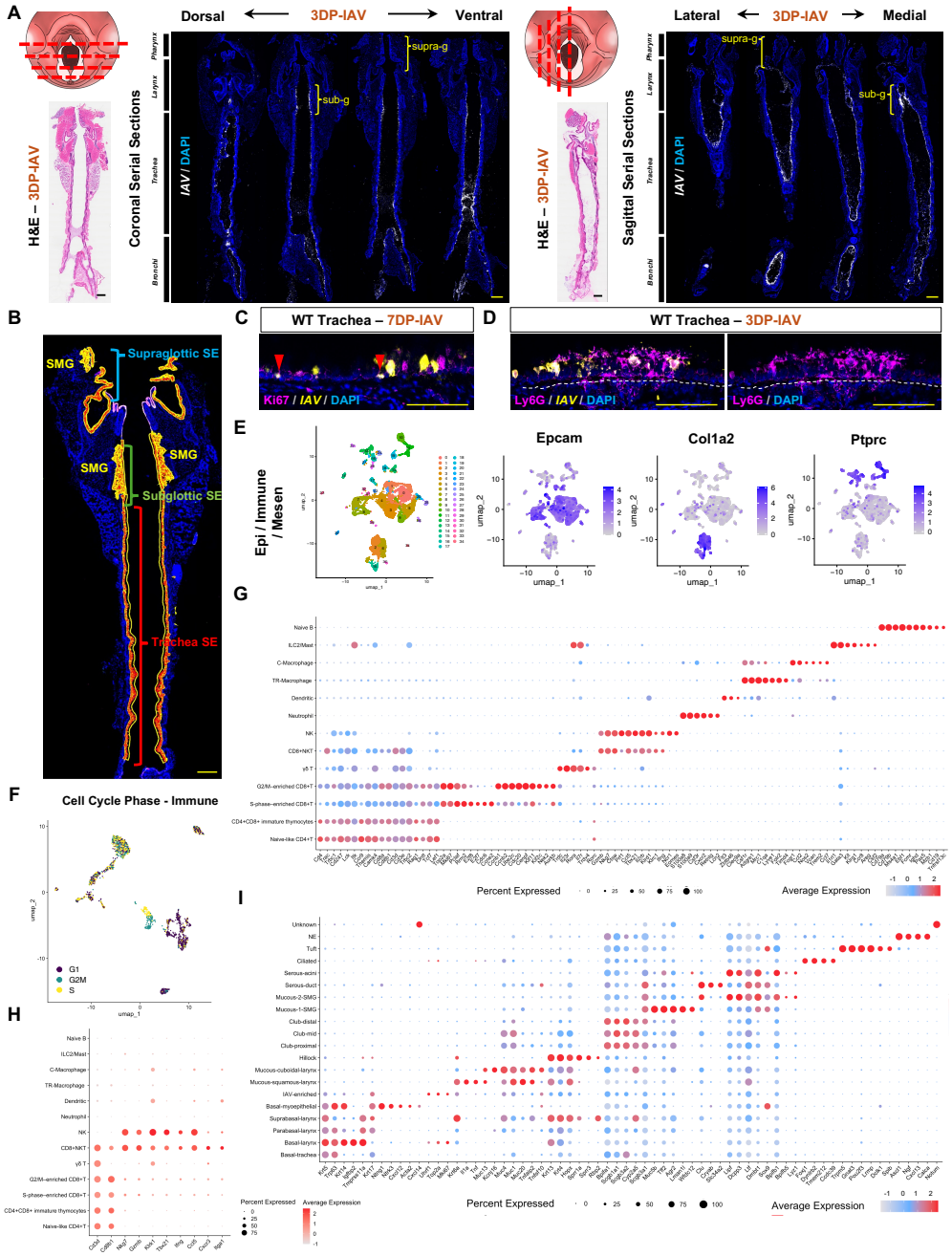

Fig S1. Spatial viral tropism and epithelial/immune cell annotation from scRNA-seq data. (A) Whole-mount coronal and sagittal sections at 3DP-IAV. (B) Coronal section schematic delineating anatomical regions used for quantification, including supraglottic and subglottic surface epithelium (SE), trachea, and submucosal glands (SMG). (C) High-magnification RNAscope/ISH of WT trachea at 7DP-IAV showing co-localization of Ki67⁺ proliferating cells with IAV mRNA. (D) High-magnification RNAscope/ISH of WT trachea at 3DP-IAV illustrating Ly6G⁺ neutrophil–associated viral containment. (E) UMAP of scRNA-seq annotated by cell type; feature plots for *Epcam*, *Col1a2*, and *Ptprc* distinguish epithelial, mesenchymal, and immune compartments. (F) Cell-cycle phase analysis of scRNA-seq immune fractions. (G) Supervised clustering with top canonical marker genes used for immune cell type annotation. (H) Dot plot of immune effector genes (dot size, percent expressed; color, average expression), highlighting cytotoxic signatures (Gzma, Gzmb, Nkg7, Ccl5) in the CD8⁺ NKT subset. (I) Supervised clustering with top canonical marker genes used for epithelial cell type annotation. DAPI, blue. Scale bars: 500 µm (A,B), 100 µm (C). All images acquired at 20× magnification. WT, wild-type; DP, days post; sub-g, subglottis; supra-g, supraglottis.

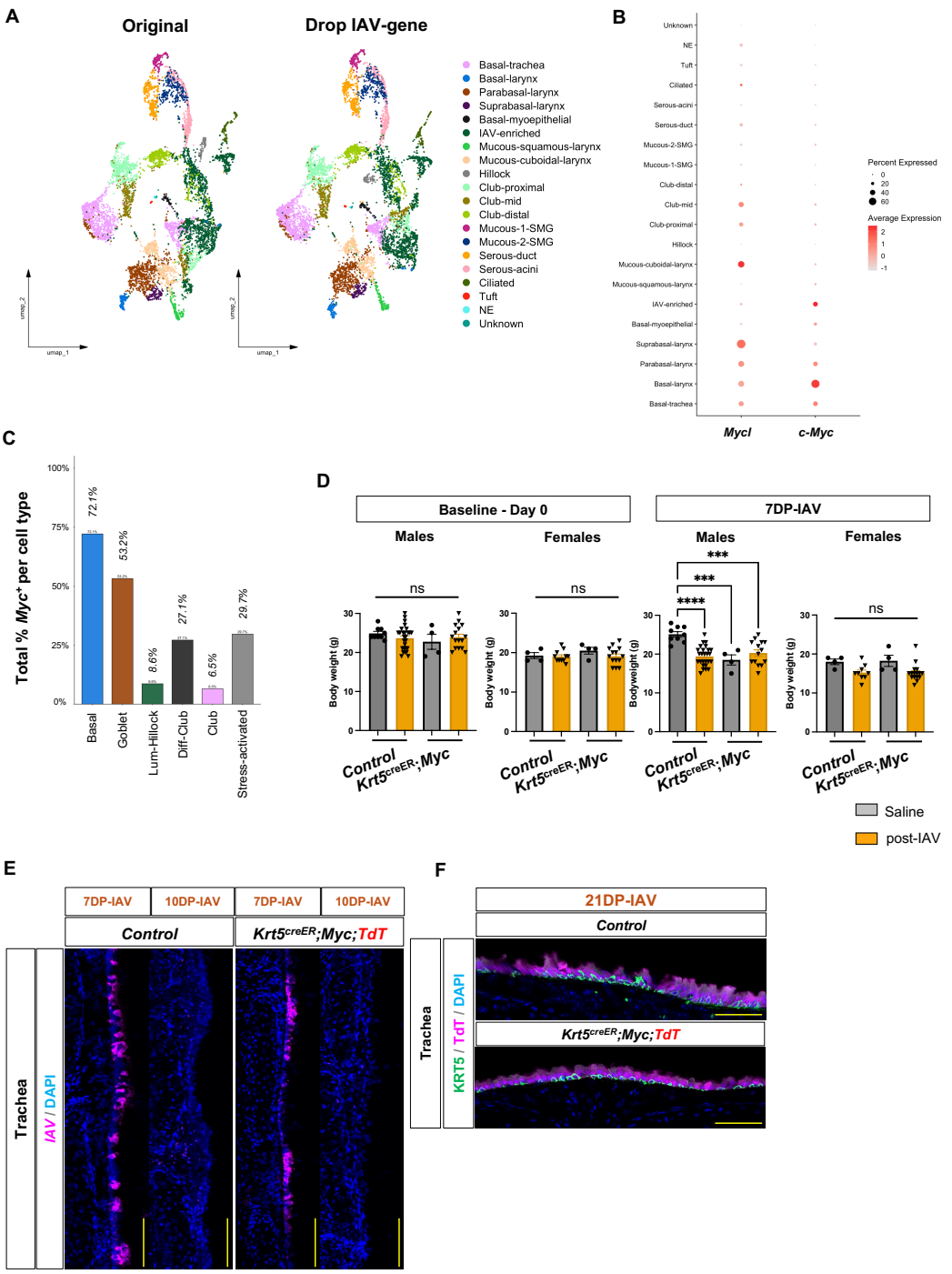

Fig S2. Validation of viral transcript integration and MYC expression in IAV-enriched airway epithelium. (A) Data-integrity check: UMAPs before and after removing the synthetic IAV transcript show identical clustering and annotations, indicating no distortion from viral transcript integration. (B) Dot plot showing *Myc* and *Mycl* expression across epithelial subtypes at 7DP-IAV; *Mycn* not found. Circle size reflects the percentage of cells expressing each gene; color indicates average expression level. (C) Quantification of the proportion of *Myc*⁺ cells within IAV-enriched epithelial populations. (D) Body weight measurements of male and female control versus Krt5creER;Myc mice at baseline (Day 0) and at 7DP-IAV; one-way ANOVA, Tukey's post-hoc analysis to compare group means, mean ± SEM. (E) RNA in situ hybridization of IAV transcripts (magenta) in tracheal sections from control and Krt5^{creER};Myc;TdT mice at 7DP-IAV and 10DP-IAV, showing comparable viral clearance kinetics between genotypes. (F) Immunofluorescence imaging of KRT5 (green) and TdTomato lineage label (magenta) at 21DP-IAV. DP days post.

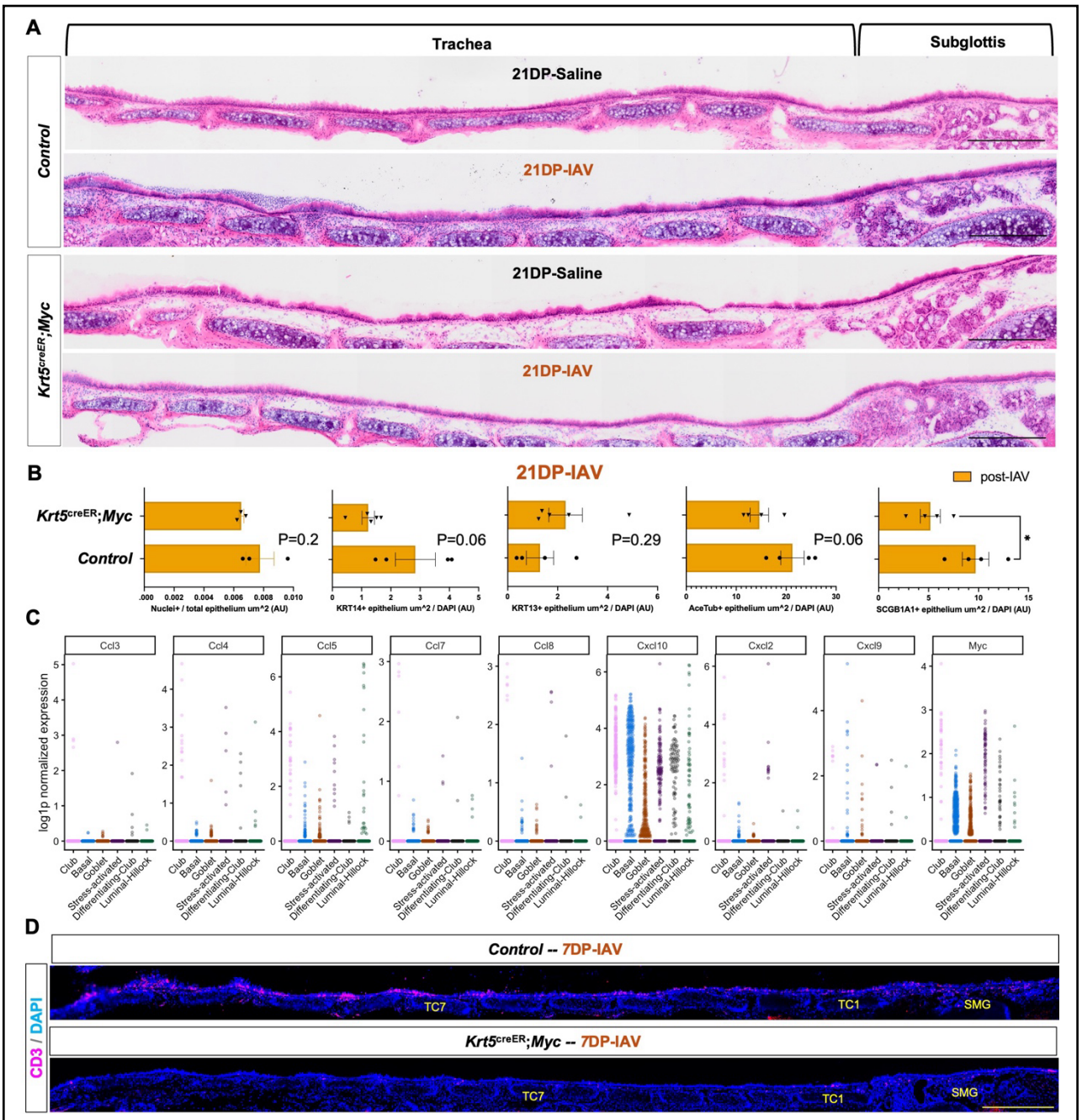

Fig S3. MYC regulates epithelial immune signaling and CD3⁺ cell accumulation following IAV infection. (A) H&E-stained coronal sections of tracheal and subglottic epithelium from control and Krt5^{creER};Myc conditional mutants at 21DP-IAV or saline treatment. (B) Quantification of total nuclei and lineage-defined epithelial compartments at 21DP-IAV, normalized to total epithelial area (um^2) and (DAPI⁺) counts, respectively. (C) Violin plots of immune-related transcripts from scRNA-seq across IAV-enriched epithelial clusters, showing differential expression of *Cd3d, Ccl4, Ccl5, Ccl7, Cd8b, Cxcl10, Cxcl2, Cxcl9*, and *Myc* at 7DP-IAV. (D) Immunofluorescence at 7DP-IAV showing reduced CD3+ cells to upper respiratory airway in *Myc* mutant mice compared to controls. Scale bars, 500 µm. *P < 0.05, **P < 0.005, ***P<0.0005; ns, not significant. DP days post.

SUPPLEMENTAL TABLES

Influenza A Virus (A/Puerto Rico/8/1934(H1N1)) reference gene sequence

ATGAAGGCAAACCTACTGGTCCTGTTATGTGCACTTGCAGCTGCAGATGCAGACACAATATGTATAGGCT
ACCATGCGAACAATTCAACCGACACTGTTGACACAGTGCTCGAGAAGAATGTGACAGTGACACACTCTGT
TAACCTGCTCGAAGACAGCCACAACGGAAAACTATGTAGATTAAAAGGAATAGCCCCACTACAATTGGGG
AAATGTAACATCGCCGGATGGCTCTTGGGAAACCCAGAATGCGACCCACTGCTTCCAGTGAGATCATGGT
CCTACATTGTAGAAACACCAAACTCTGAGAATGGAATATGTTATCCAGGAGATTTCATCGACTATGAGGA
GCTGAGGGAGCAATTGAGCTCAGTGTCATCATTCGAAAGATTCGAAATATTTCCCAAAGAAAGCTCATGG
CCCAACCACAACACAACCAAAGGAGTAACGGCAGCATGCTCCCATGCGGGGAAAAGCAGTTTTTACAGAA
ATTTGCTATGGCTGACGGAGAAGGAGGGCTCATACCCAAAGCTGAAAAATTCTTATGTGAACAAGAAAGG
GAAAGAAGTCCTTGTACTGTGGGGTATTCATCACCCGTCTAACAGTAAGGATCAACAGAATATCTATCAG
AATGAAAATGCTTATGTCTCTGTAGTGACTTCAAATTATAACAGGAGATTTACCCCGGAAATAGCAGAAA
GACCCAAAGTAAGAGATCAAGCTGGGAGGATGAACTATTACTGGACCTTGCTAAAACCCGGAGACACAAT
AATATTTGAGGCAAATGGAAATCTAATAGCACCAAGGTATGCTTTCGCACTGAGTAGAGGCTTTGGGTCC
GGCATCATCACCTCAAACGCATCAATGCATGAGTGTAACACGAAGTGTCAAACACCCCTGGGAGCTATAA
ACAGCAGTCTCCCTTTCCAGAATATACACCCAGTCACAATAGGAGAGTGCCCAAAATACGTCAGGAGTGC
CAAATTGAGGATGGTTACAGGACTAAGGAACATTCCGTCCATTCAATCCAGAGGTCTATTTGGAGCCATT
GCCGGTTTTATTGAAGGGGGATGGACTGGAATGATAGATGGATGGTACGGTTATCATCATCAGAATGAAC
AGGGATCAGGCTATGCAGCGGATCAAAAAAGCACACAAAATGCCATTAACGGGATTACAAACAAGGTGAA
CTCTGTTATCGAGAAAATGAACATTCAATTCACAGCTGTGGGTAAAGAATTCAACAAATTAGAAAAAAGG
ATGGAAAATTTAAATAAAAAAGTTGATGATGGATTTCTGGACATTTGGACATATAATGCAGAATTGTTAG
TTCTACTGGAAAATGAAAGGACTCTGGATTTCCATGACTCAAATGTGAAGAATCTGTATGAGAAAGTAAA
AAGCCAATTAAAGAATAATGCCAAAGAAATCGGAAATGGATGTTTTGAGTTCTACCACAAGTGTGACAAT
GAATGCATGGAAAGTGTAAGAAATGGGACTTATGATTATCCCAAATATTCAGAAGAGTCAAAGTTGAACA
GGGAAAAGGTAGATGGAGTGAAATTGGAATCAATGGGGATCTATCAGATTCTGGCGATCTACTCAACTGT
CGCCAGTTCACTGGTGCTTTTGGTCTCCCTGGGGGCAATCAGTTTCTGGATGTGTTCTAATGGATCTTTG
CAGTGCAGAATATGCATCTGA

Clustering fidelity analysis results before and after exclusion of synthetic IAV-gene

ARI:NMI Confusion Matrix

	DropIAV					
Original	**1**	**10**	**11**	**12**	**13**	**14**
1	**1123**	**0**	**0**	**0**	**0**	**0**
10	**0**	**342**	**0**	**0**	**0**	**0**
11	**0**	**0**	**269**	**0**	**0**	**0**
12	**0**	**0**	**0**	**162**	**0**	**0**
13	**0**	**0**	**0**	**0**	**148**	**0**
14	**0**	**0**	**0**	**0**	**0**	**131**

m2; r_proc

m2	0.000126119
r_proc	0.9999369

Percentage of cells expressing "IAV reference gene" within each major cell compartment and cell type

Gene	Pharyngolaryngeal %	Tracheobronchial %	Submucosal %	IAV-enriched %
Tmprss11a+	64.87576	10.6769	2.629544	12.24242
Nkx2-1+	15.17797	60.36288	33.79737	33.57576
Dmbt1+	35.93015	42.63782	90.719258	26.9697

Gene	CellType	Total cells_Control	Total cells_post-IAV	CellType expressing IAV-gene %
IAV-gene	Club-proximal	486	170	10.21
IAV-gene	Club-distal	290	121	6.81
IAV-gene	Club-mid	291	120	10.95
IAV-gene	Basal-trachea	847	282	4.96
IAV-gene	Serous-acini	328	73	3.49
IAV-gene	Mucous-1-SMG	91	71	11.73
IAV-gene	Ciliated	67	64	28.24
IAV-gene	Mucous-cuboidal-larynx	208	241	16.48
IAV-gene	Mucous-2-SMG	191	117	7.14
IAV-gene	Parabasal-larynx	247	387	13.56
IAV-gene	Serous-duct	152	194	14.45
IAV-gene	Mucous-squamous-larynx	35	115	38.00
IAV-gene	IAV-enriched	152	1498	32.12
IAV-gene	Suprabasal-larynx	53	71	8.87
IAV-gene	Basal-larynx	73	59	5.30
IAV-gene	Hillock	56	40	7.29
IAV-gene	Basal-myoepithelial	34	42	15.79
IAV-gene	Tuft	20	0	0.00
IAV-gene	NE	5	0	0.00
IAV-gene	Unknown	1	6	14.29

Percentage of cells in S or G2M phase for each epithelial cluster

CellType	total_cells	cycling_cells	percentage_cycling
Basal-trachea	1129	300	26.572188
Basal-larynx	132	84	63.636364
Parabasal-larynx	634	129	20.347003
Suprabasal-larynx	124	9	7.258065
Basal-myoepithelial	76	18	23.684211
IAV-enriched	1650	1197	72.545455
Mucous-squamous-larynx	150	27	18
Mucous-cuboidal-larynx	449	48	10.690423
Hillock	96	36	37.5
Club-proximal	656	133	20.27439
Club-mid	411	56	13.625304
Club-distal	411	218	53.041363
Mucous-1-SMG	162	15	9.259259
Mucous-2-SMG	308	37	12.012987
Serous-duct	346	47	13.583815
Serous-acini	401	99	24.688279
Ciliated	131	55	41.984733
Tuft	20	4	20
NE	5	0	0
Unknown	7	0	0

REAGENT or RESOURCE

REAGENT or RESOURCE	SOURCE	IDENTIFIER
Antibodies		
Rabbit-KRT5	Abcam	Cat#ab52635
Rabbit, anti-KRT13	Abcam	Cat#ab92551
Mouse, anti-KRT14	Millipore	Cat#CBL197
Rabbit, anti-KRT17	Santa Cruz Biotechnology	Cat#sc-393002
Mouse-aSMA-FITC	Millipore Sigma	Cat#F3777
Rat-CD3	Abcam	Cat#ab11089
Rat-Ly6G	BioLegend	Cat#127601
Mouse-RFP	Abcam	Cat#ab125244
Rabbit-DsRed	Takara Clontech	Cat#632496
Mouse-FOXJ1	eBioscience/Fisher	Cat#5013931
Mouse-Acetylated tubulin	Sigma	Cat#T7451
Rabbit-SCGB1A1	Abcam	Cat#ab213203
Goat anti-Rabbit IgG Alexa Flour 488	ThermoFisher	Cat#A27034
Goat anti-mouse IgG, Cy3™	Jackson Immuno Research	Cat#115-166-003
Goat anti-rat IgG, Cy3™	Jackson Immuno Research	Cat#112-165-003
BV510-conjugated anti-CD45	BioLegend	Cat#103138
APC-FITC-conjugated anti-Epcam	BioLegend	Cat#118214
PE-conjugated anti-CD31	BioLegend	Cat#102508
CD11b: Brilliant Violet 450	BioLegend	Cat#75-0112-U025
Mm-*IAV*	Advanced Cell Diagnostics	Cat#521181
Mm-*Myc*	Advanced Cell Diagnostics	Cat#413451
Mm-*Cxcl10*	Advanced Cell Diagnostics	Cat#408921

Mm-*tdTomato*	Advanced Cell Diagnostics	Cat#317041
Mm-*Gzmb*	Advanced Cell Diagnostics	Cat#490191
Mm-*Ccl5*	Advanced Cell Diagnostics	Cat#469601
Bacterial and virus strains		
Influenza strain A/H1N1/PR/8	ATCC	VR-95PQ
Chemicals, peptides, and recombinant proteins		
Tamoxifen	Sigma-Aldrich	Cat#T-5648-1G
RPMI 1640 Medium	Thermo Scientific	Cat#11875093
1 mM HEPES	Life Technology	Cat#15630080
Dispase	Roche	Cat#4942086001
DNase I	Roche	Cat#11284932001
1 mM CaCl2	Sigma-Aldrich	Cat#21115
1 mM MgCl2	Sigma-Aldrich	Cat#20303M
Collagenase D	Roche	Cat#11088858001
RBC Lysis Buffer	BioLegend	Cat#420301
Critical commercial assays		
RNAscope® Multiplex Fluorescent Reagent Kit V2	Advanced Cell Diagnostics	Cat#323100
Click-it TUNEL Alexa Flour 488	ThermoFisher	Cat#C10245
Click-it EdU Alexa Flour 488	ThermoFisher	Cat#C10337
Deposited data		
Single cell RNA-seq data for mouse larynx/trachea	Gene Expression Omnibus	n/a
bulk RNA-seq data for mouse larynx/trachea	Gene Expression Omnibus	n/a
Experimental models: Organisms/strains		
Mouse: Wildtype C57BL/6J	Jackson laboratory	JAX: 000664
Mouse: Rosa-lxl-tdTomato (Ai14)	Jackson laboratory	JAX: 007914
Mouse: Ascl1-creERT2	Jackson laboratory	JAX: 012882
Mouse: Krt5-creERT2	Jackson laboratory	JAX: 029155
Mouse: Myc-flox	Gifted from Rob Signer at UCSD	MMRRC 036778
Software and algorithms		
RStudio (v2024.12.1+563)	RStudio Team	http://www.rstudio.com/
R (v4.5.0)	R Core Team	https://www.R-project.org/
Cell Ranger (v3.0.2)	10x Genomics	https://support.10xgenomics.com/ single-cell-gene-expression/software/ pipelines/latest/what-is-cell-ranger